Computational Particle Mechanics (2023) 10:155–172
https://doi.org/10.1007/s40571-022-00487-5

Computational assessment of immersed boundary–lattice Boltzmann method for complex moving boundary problems

Sambit Majumder[1,2] · Arnab Ghosh[1,3] · Dipankar Narayan Basu[1] · Ganesh Natarajan[4]

Received: 25 January 2022 / Revised: 17 April 2022 / Accepted: 7 May 2022 / Published online: 15 June 2022

Abstract
In the present work, we investigate the accuracy and robustness of our in-house OpenMP parallelized direct-forcing immersed boundary–lattice Boltzmann (DF-IB-LB) solver by undertaking studies on accuracy, discrete conservation, Galilean invariance and quantification of spurious force oscillations (SFO). Our study reveals that DF-IB-LB exhibits first and second-order spatial accuracy for velocity and pressure errors, respectively, for generic moving boundary problems. The method is found to be Galilean invariant, while errors in discrete conservation and SFO decay linearly and superlinearly, respectively, with grid refinement. The numerical simulations with the proposed solver on a vast number of complex moving boundary problems involving imposed and induced motion highlight its efficacy as a fast, robust and accurate framework for single-phase flows with and without fluid–particle interactions.

Keywords Immersed boundary–lattice Boltzmann · Spurious force oscillations · Moving boundary

1 Introduction

Numerical simulations of fluid–particle interaction applications, particularly moving body applications, have gained attention over the last two decades owing to their ability to deliver valuable insights in engineering, bio-medical and environmental technologies, among other fields. Some of the notable examples include fluidization of particles [1,2], microfluidic and biomedical applications [3,4], multiphase flows [5], pollution control [6], food processing [7], additive manufacturing [8], granular suspension [9] and sedimentation [10–12]. The traditional use of body-fitted methods for such moving boundary applications, while higher-order accurate, is computationally expensive and sometimes even requires re-meshing. Immersed boundary methods (IBM) [13] (also known as non-body-conformal grid methods) have established themselves as a promising alternative for such scenarios and can be coupled with frameworks such as finite-difference, finite-volume, finite-element and lattice-Boltzmann method. In the present work, we consider the lattice-Boltzmann method (LBM) due to its locality of operation owing to the mesoscopic treatment, inherent parallelizable nature and simplicity of the algorithm.

Coupled Immersed boundary–lattice Boltzmann (IB-LB) [14] formulations employ a non-body conformal grid with the complex boundary represented by a set of Lagrangian points while immersed into an Eulerian fluid domain. Upon solving the governing equation on Eulerian nodes, various flow field parameters such as velocity, pressure, and temperature are spread to Lagrangian boundary nodes. The resulting force that evolves out of particle motion and fluid–particle interactions at Lagrangian nodes can now be distributed into Eulerian fluid nodes while simultaneously advecting the Lagrangian nodes to account for the motion of the body. Among several immersed boundary–lattice

✉ Ganesh Natarajan
n.ganesh@iitpkd.ac.in

Sambit Majumder
sambit.majumder@iitg.ac.in

Arnab Ghosh
arnabghosh.sphs@gmail.com

Dipankar Narayan Basu
dnbasu@iitg.ac.in

[1] Department of Mechanical Engineering, Indian Institute of Technology Guwahati, Guwahati, Assam 781039, India

[2] Department of Mechanical Engineering, National Institute of Technology Meghalaya, Shillong, Meghalaya 793003, India

[3] Department of Applied Physics, Eindhoven University of Technology, 5612 AZ Eindhoven, The Netherlands

[4] Department of Mechanical Engineering, Indian Institute of Technology Palakkad, Palakkad, Kerala 678557, India

Boltzmann methodologies (IB-LB) in open literature, we briefly review some of the prominent variants. These include the penalty-force method [15], direct forcing IB-LB method [16], momentum-exchange-based method [17], velocity correction method [18] and partially saturated computational cells method [19] and is definitely not an exhaustive list. Feng and Michaelides [15] formulated the penalty-force method in a Lagrangian–Eulerian framework which considers deformable particles with a high stiffness coefficient and adds to the evolution equation an external force density term that accounts for fluid and particle velocity field. This approach was used to study a couple of fluid–particle interaction problems—DKT motion of two particles and sedimentation of multiple particles, from which the authors concluded that coupled IB-LB method is capable of accurately resolving fluid–particle boundary condition. They also found that the method is more accurate than bounce-back schemes and reduces initial fluctuations in particle forces and torques, which are common in general LBM approaches. The penalty-force approach, however, suffers the limitation that it requires a careful choice of user-defined free parameters. Leveraging the advantages of both LBM and IBM, which includes Eulerian mesh for fluid domain and Lagrangian nodes for solid moving boundaries, Niu et al. [17] introduced a direct-forcing term based on momentum-exchange where particle distribution functions on the boundary are evaluated using interpolation of Lagrangian polynomial from Eulerian mesh. Since conventional IB-LB only approximately satisfies the no-slip on surfaces, Wu and Shu [18] introduced the velocity-correction-based IB-LB formulation where the velocity correction at Eulerian nodes is spread from the corrected velocity term at Lagrangian boundary nodes and simultaneously imposes a no-slip boundary condition on the solid bodies. Zhang et al. [20] formulated an iterative force correction method to obtain external force term involved in the LB equation that can accurately implement no-slip boundary conditions on solid boundaries considering the effects of present and next time steps. They employed Lagrangian polynomial interpolations instead of the Dirac delta function to determine velocities on boundaries from neighboring fluid nodes. Of specific interest to the present study is the DF-IB-LB introduced by Feng and Michaelides [16] where a forcing term in the LB governing equation is included, which can enforce no-slip boundary condition on the immersed surface and eliminate the necessity of using free-parameters unlike those in their earlier approach [15]. Their work highlighted the capability of the approach to offer a smooth computational boundary as compared to the conventional "bounce-back" schemes used in LBM. While they remarked that the DF-IB-LB method possesses the same order of accuracy as the LB method, no quantitative data were provided to support this claim. Subsequently, Dupuis et al. [21] introduced the interpolating forcing approach that exhibited an order of accuracy of 1.9 in drag coefficients of an impulsively started cylinder as compared to a 1.5 convergence rate using direct-forcing method. Although the interpolating forcing approach is a nearly second-order accurate method, it involves tedious interpolations, which in turn increases the computational cost and time for moving boundary problems.

Our present study focuses on the DF-IB-LB method, which is attractive owing to its simple algorithm but can achieve comparable accuracy as other aforementioned variants of IB-LB methods. While this method has been proposed as an efficient framework to solve incompressible hydrodynamic problems, a thorough analysis of the approach with regard to pivotal aspects like discrete mass conservation, Galilean invariance, and spurious force oscillations in moving boundary problems has been lacking to the best of the authors' knowledge. Therefore, the current investigations are targeted toward a comprehensive evaluation of the DF-IB-LB approach with a specific focus on the following objectives.

1. Studies on spatial order of accuracy for moving boundary problems.
2. Discrete conservation study and the role of relaxation factor τ.
3. Galilean invariance study of the algorithm
4. Dependence of lattice resolution on spurious force fluctuations of force signals.

We also carry out numerical simulations over a broad spectrum of moving boundary problems involving single and multiple bodies with imposed and induced motion to benchmark the approach and we believe that this extensive assessment and analysis of the DF-IB-LB method is a novel contribution that can be beneficial to the computational LB community.

The remainder of the manuscript is organized as follows. The mathematical formulation involving LB methodology, direct forcing IB-LB method, and incorporation of particle motion dynamics is presented in Sect. 2. The next Sect. 3 presents studies on the accuracy, discrete conservation, Galilean invariance, and dependence of grid resolution on spurious force fluctuation in moving boundary problems using the DF-IB-LB method. The efficacy and robustness of the DF-IB-LB method for accurate prediction of fluid–particle hydrodynamic interaction problems are illustrated by carefully examining its viability for a wide spectrum of moving boundary problems in Sect. 4. The salient conclusions from our investigations are finally summarized in Sect. 5.

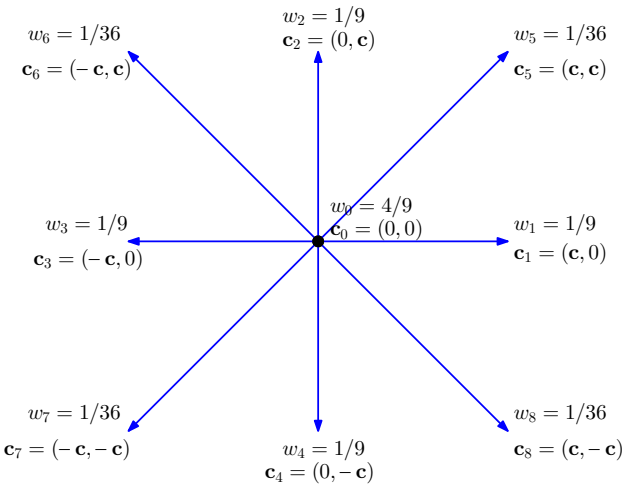

Fig. 1 Schematic showing velocity direction $\vec{c}_i$ and corresponding weights (w_i) for a D_2Q_9 lattice arrangement

2 Mathematical formulation

2.1 Basic LBM formulation

The lattice Boltzmann method uses sets of particle distribution function (f), which signifies the probability to find particles at a location at a particular instant. The discrete incompressible D_2Q_9 LBGK equation along a specified direction (Fig. 1) can be written as:

$$f_i(\vec{x} + \vec{c}_i \Delta t, t + \Delta t) = f_i(\vec{x}, t) + \Omega_i^{\mathrm{BGK}} \tag{1}$$

where Ω_i^{BGK} and τ are the BGK collision operator and the relaxation parameter, respectively, related as:

$$\Omega_i^{\mathrm{BGK}} = \frac{\Delta t}{\tau}(f_i^{\mathrm{eq}}(\vec{x}, t) - f_i(\vec{x}, t)) \tag{2}$$

f_i^{eq} is the local equilibrium distribution function.

$$f_i^{\mathrm{eq}}(\vec{x}, t) = w_i \left[\rho(\vec{x}, t) + \frac{\vec{c}_i.\vec{u}}{{c_s}^2} + \frac{1}{2}\frac{(\vec{c}_i.\vec{u})^2}{{c_s}^4} - \frac{1}{2}\frac{(\vec{u}.\vec{u})}{{c_s}^2} \right] \tag{3}$$

where c_s is the sonic velocity in the lattice dimension given as $c_s = c/\sqrt{3}$, c is the lattice velocity $(= \Delta x/\Delta t)$ corresponding to the adopted grid spacing (Δx) and time step (Δt) and w_i is the weight function in the respective direction. The kinematic viscosity of the fluid (ν_f) is related to the relaxation factor τ as in Eq. (4), which is a manifestation of recovered Navier–Stokes equation via multi-scale Chapman Enskog expansion [22].

$$\nu_f = \left(\tau - \frac{\Delta t}{2}\right)\frac{c^2}{3} \tag{4}$$

Here, the left-hand side term of Eq. (1) represents advection (streaming), and right-hand side term represents collision. Macroscopic quantities like density and velocity can be obtained by taking velocity moments of particle distribution function as:

$$\rho(\vec{x}, t) = \sum_i f_i \tag{5}$$

$$\vec{u}(\vec{x}, t) = \sum_i f_i \vec{c}_i \tag{6}$$

2.2 Direct forcing IB-LB formulation

The fully explicit nature of the discretized LB equation offers advantages like locality of operations, ease of parallelization, and algorithm simplicity. Despite such benefits, conventional treatment of boundary conditions [22,23] in LBM instigates spuriousness in hydrodynamic forces at the fluid–particle interface, further necessitating to use specialized techniques such as the refill-algorithm [24,25] to mitigate the same. The limitations of the conventional LBM can be overcome by coupling Immersed Boundary (IB)–Lattice Boltzmann method (LB) [15,16]. In this case, the discretized governing equation (Eq. 7) is solved at Eulerian lattice nodes, from where information (in terms of pressure, velocity, temperature, etc.) is interpolated to immersed Lagrangian nodes as shown in Fig. 2.

Hydrodynamic forces experienced by the body due to its motion and fluid–particle interactions are computed at Lagrangian boundary nodes, which are then suitably redistributed onto the Eulerian nodes in the fluid regime. The DF-IB-LB method modifies the LB governing Eq. (1) as:

$$f_i^{'} = f_i(\vec{x}, t) + \Omega_i^{\mathrm{BGK}} + F_i \Delta t \tag{7}$$

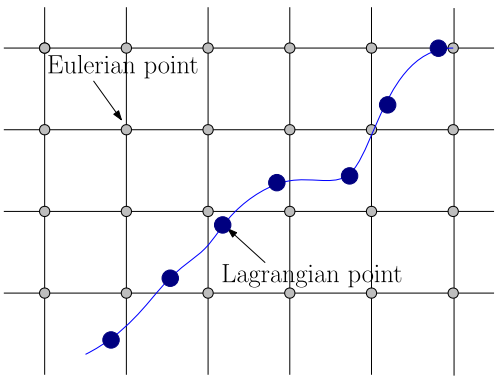

Fig. 2 Illustration of the Immersed Boundary method. The Lagrangian points represent the boundary, and the intersection of the mesh lines represent the Eulerian fluid points

The direct forcing term ($\vec{F}_i$) in Eq. (7) can be expressed as:

$$F_i = \left(1 - \frac{1}{2\tau}\right)\omega_i \left(\frac{\vec{c}_i - \vec{u}}{c_s^2} + \frac{\vec{c}_i.\vec{u}}{c_s^2}\vec{c}_i\right).\vec{F}_b \tag{8}$$

where $\vec{F}_b(\vec{x}, t)$ is the fluid body force density. Once we obtain the non-forced velocity at the Lagrangian nodes, we can calculate the particle boundary force density at the m^{th} Lagrangian node at position $\vec{X}_m$ using Eq. (9).

$$\vec{F}(\vec{X}_m, t) = \frac{2}{\Delta t}[\vec{U}^d(\vec{X}_m, t) - \vec{U}^*(\vec{X}_m, t)] \tag{9}$$

where $\vec{U}^d$ is the desired velocity at the Lagrangian point, and $\vec{U}^*$ is the interpolated fluid velocity at the Lagrangian node obtained from Eq. (10).

$$\vec{U}^*(\vec{X}_m, t) = \sum_{i,j} \vec{u}^*(\vec{x}, t)\delta_h(\vec{x} - \vec{X}_m)h^2 \tag{10}$$

The non-forced fluid velocity $\vec{u}^*$ at the Eulerian nodes is obtained using Eq. (6), and the particle boundary force density $\vec{F}(\vec{X}_m, t)$ is spread to neighboring Eulerian nodes as:

$$\vec{F}_b(\vec{x}, t) = \sum_m \vec{F}(\vec{X}_m, t)\delta_h(\vec{x} - \vec{X}_m)\Delta s \tag{11}$$

where Δs is the arc length. $\delta_h(\vec{x}_{ij} - \vec{X}_m)$ is a continuous kernel function which approximates the Dirac Delta function as:

$$\delta_h(\vec{x} - \vec{X}_m) = \frac{1}{h^2}\phi\left(\frac{x - X_m}{h}\right)\phi\left(\frac{y - Y_m}{h}\right) \tag{12}$$

where h is mesh spacing. Δs should be adopted such that it averts mass-leakage and ensures no-slip boundary condition. Peskin [26] proposed $\Delta s \leq h/2$ and Cheng et al. [27] suggested $\Delta s < h$ for obtaining accurate results. In the present study, number of Lagrangian nodes over the particle's surface is adopted as 1.2 times (C/h), where C is the circumference of the particle. It leads to $\Delta s \approx 0.83h$.

Finally, the velocity is updated according to Eq. (13) that reads

$$\vec{u}(\vec{x}, t) = \vec{u}^*(\vec{x}, t) + 0.5\vec{F}_b\Delta t \tag{13}$$

2.3 Incorporation of particle dynamics

Accurate estimation of hydrodynamic forces and moments on the solid structure due to the fluid is crucial in any fluid–structure interaction problem. Traditional use of momentum exchange method [28,29] and stress integration method [23] to evaluate surface forces in LBM require complicated and hectic interpolations of the distribution function. A moving boundary scenario further instills complications to tackle birth and death of solid-fluid nodes using refill algorithms [24,25] at every time step. In the DF-IB-LB method, the total hydrodynamic force can be obtained by summing Eq. (9) over m-Lagrangian nodes.

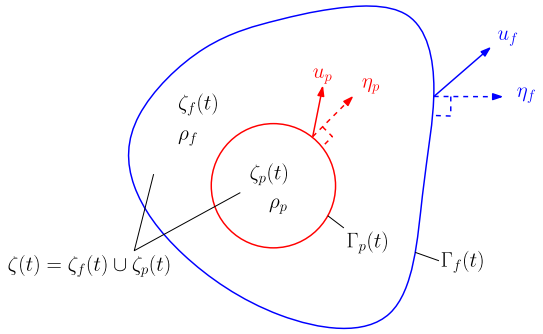

Fig. 3 Time varying control surface ($\Gamma_p(t)$ and $\Gamma_f(t)$) and its corresponding control volumes ($\zeta_p(t)$ and $\zeta_f(t)$)

To appreciate the procedure of force evaluation using DF-IB-LB method, consider a solid particle of surface area $\Gamma_p(t)$ and volume $\zeta_p(t)$ immersed into a control volume of surface area $\Gamma_f(t)$ and volume $\zeta_f(t)$, as depicted in Fig. 3. The arbitrary velocity vectors and outward normal surface vectors of respective surfaces are also depicted. The total surface force exerted by fluid onto the particle ($f \rightarrow p$) can be evaluated by integrating the forces over the surface area of particle (Γ_p) as:

$$\vec{F}_{f\rightarrow p} = -\int_{\Gamma_p} \left[\rho\vec{u}\left(\vec{u} - \vec{u}_p\right) + \sigma\right] \cdot \vec{\eta}_p \, \mathrm{d}\Gamma \tag{14}$$

where σ represents the viscous stress tensor. The fluid mass is considered to be constrained by control surfaces Γ_p and Γ_f at this particular instant. Following Cauchy's stress principle, the conservation of linear momentum can be expressed as:

$$\begin{aligned}\frac{\partial}{\partial t}\int_{\zeta_f} \rho\vec{u} \, \mathrm{d}\zeta = &-\int_{\Gamma_f} \left[\rho\vec{u}\left(\vec{u} - \vec{u}_f\right) + \sigma\right] \cdot \vec{\eta}_f \, \mathrm{d}\Gamma \\ &- \int_{\Gamma_p} \left[\rho\vec{u}\left(\vec{u} - \vec{u}_p\right) + \sigma\right] \cdot \left(-\vec{\eta}_p\right) \, \mathrm{d}\Gamma\end{aligned} \tag{15}$$

which can further be combined with Eq. (14) to yield

$$\frac{\partial}{\partial t}\int_{\zeta_f} \rho\vec{u} \, \mathrm{d}\zeta = -\vec{F}_{f\rightarrow p} - \int_{\Gamma_f} \left[\rho\vec{u}\left(\vec{u} - \vec{u}_f\right) + \sigma\right] \cdot \vec{\eta}_f \, \mathrm{d}\Gamma \tag{16}$$

The resulting equation for the conservation of linear momentum for the whole domain, including both solid (ζ_p) and fluid volumes (ζ_f), can similarly be expressed as:

$$\frac{\partial}{\partial t}\int_{\zeta_f\cup\zeta_p}\rho\vec{u}\,\mathrm{d}\zeta = -\int_{\Gamma_f}\left[\rho\vec{u}\left(\vec{u}-\vec{u}_f\right)+\sigma\right]\cdot\vec{\eta}_f\,\mathrm{d}\Gamma + \int_{\zeta_f\cup\zeta_p}\vec{F}\,\mathrm{d}\zeta \tag{17}$$

with $\vec{F}$ corresponding to the fluid–particle interaction force. Therefore, the surface force acting on the particle due to the momentum interaction with the neighboring fluid can be obtained by subtracting Eq. (16) from Eq. (17), as follows:

$$\vec{F}_{f\to p} = \underbrace{\frac{\partial}{\partial t}\int_{\zeta_p}\rho\vec{u}\,\mathrm{d}\zeta}_{\text{added mass}} - \int_{\zeta_f\cup\zeta_p}\vec{F}\,\mathrm{d}\zeta \tag{18}$$

Consideration of the virtual mass (added mass) effect, appearing as the first term on the right-hand side of Eq. (18), is of paramount importance in moving boundary problems. It signifies the increase in inertia of the fluid adjacent to the particle during its motion and therefore is relevant solely for accelerating bodies and fluid nodes in proximity to the surface. Thus, the added mass term can be substituted by the acceleration experienced by a virtual fluid element having an identical volume to the particle (ζ_p) and desired center-of-mass velocity ($\vec{U}^d$).

$$\vec{F}_{f\to p} = \rho\zeta_p\frac{\partial\vec{U}^d}{\partial t} - \int_{\zeta_f\cup\zeta_p}\vec{F}\,\mathrm{d}\zeta \tag{19}$$

For a non-accelerating particle, the first term on the right-hand side of the Eq. (19) vanishes, resulting in a simple numerical integration of boundary forces, regardless of the position of the particle.

$$\int_{\zeta_f\cup\zeta_p}\vec{F}\,\mathrm{d}\zeta \approx \sum\vec{F}\Delta x^D \tag{20}$$

where D stands for the dimension of the problem. Following Newton's linear and angular momentum conservation principles, the translational velocity of the particle can be obtained for the added mass formulation as:

$$\rho_p\zeta_p\frac{\mathrm{d}\vec{\mathrm{U}}^{\mathrm{d}}}{\mathrm{d}t} = -\vec{F}_{f\to p} + \left(\rho_p-\rho_f\right)\zeta_p\vec{g} + \vec{F}^c \tag{21}$$

where $\vec{F}^c$ represents the particle–particle and particle–wall collision, which is conceived following the work of Feng and Michaelides [16]. The angular momentum conservation can be expressed by taking a moment over Eq. (21), neglecting $\vec{F}^c$ in the present study, as:

$$I_p\frac{\mathrm{d}\vec{\Omega}_p}{\mathrm{d}t} = \frac{\partial}{\partial t}\int_\zeta\left(\vec{x}_p-\vec{x}_c\right)\times\rho_f\vec{u}_c\,\mathrm{d}\zeta - \int_\zeta\left(\vec{x}_p-\vec{x}_c\right)\times\vec{F}\,\mathrm{d}\zeta \tag{22}$$

where I_p, $\vec{\Omega}_p$, $\vec{x}_p$ and $\vec{x}_c$ denote the mass moment of inertia, angular velocity, position vectors of the interfacial point, and the reference point, respectively. The position and surface velocity can now be updated using

$$\frac{\mathrm{d}\vec{X}_c}{\mathrm{d}t} = \vec{U}^d \tag{23a}$$

$$\vec{u}_p\left(\vec{X}_p\right) = \vec{u}_c + \vec{\Omega}_p\times\left(\vec{X}_p-\vec{X}_c\right) \tag{23b}$$

It must be noted that we have used the first-order Euler explicit method for numerically evaluating the temporal derivatives of Eqs. (21), (22) and (23a), and that the net interfacial force can be resolved considering momentum transfer involving each of the Lagrangian nodes of the particle,

$$\int_{\zeta_f\cup\zeta_p}\vec{F}\mathrm{d}\zeta \approx \sum_m\vec{F}(\vec{X}_m,t)\Delta\Gamma_p(\vec{X}_m,t)\Delta x \tag{24}$$

where $\Delta\Gamma_p$ is the area (or arc length in 2D) of the surface at a Lagrangian point $\vec{X}_m$ on the particle.

3 Evaluation of DF-IB-LB algorithm

In this section, we present the analysis of the DF-IB-LB method on four aspects—accuracy, discrete conservation, Galilean invariance, and quantification of spurious force oscillations. While several studies discuss the accuracy of the DF-IB-LB method, there are no known studies that have investigated the ability of the DF-IB-LB method to conserve mass and momentum at the discrete level, assess its Galilean invariance and determine spurious force oscillations associated with aerodynamic force coefficients in moving boundary problems. These studies are expected to further shed light on aspects of the DF-IB-LB methodology that have hitherto not been explored in the literature, but are of paramount importance for the practical viability of the approach.

3.1 Discrete conservation study

The appraisal of discrete conservation properties is an important aspect pertaining to the IB-LB method. Yin et al. [30] showed that the artificial treatment of local mass conservation at fluid–solid interface is extraneous in conventional LB boundary condition schemes and could pollute the accuracy of solution in fluid–structure interaction problems. We study the global mass flux error in simulation using the DF-IB-LB on curved boundary problems and show that it remains at acceptable levels despite any ancillary treatment at the solid–fluid interface. In this section, we consider the flow through a curved channel which is immersed into the underlying regular Cartesian mesh in a computational domain of

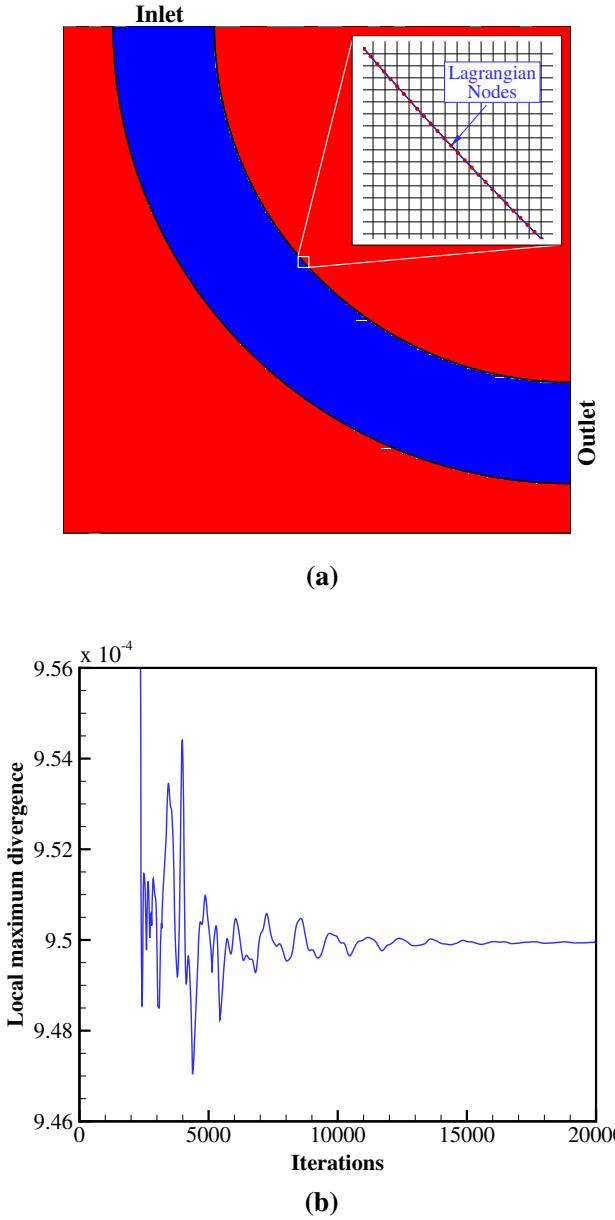

Fig. 4 **a** Schematic representation of the computational domain with a flow through curved channel. **b** Time history of local maximum divergence in flow through curved channel

size $L \times L$. The boundaries of the curved channel are not aligned with the mesh, and its inner and outer radii are $0.7L$ and $0.9L$, respectively, as depicted in Fig. 4a. Following a similar study for immersed boundary methods in the finite volume framework by Patel and Natarajan [31], we choose $L = 400$, 500, 600 and 800 and impose a uniform velocity at the inlet while a constant pressure and zero normal velocity gradient is prescribed at the outlet. Studies are performed for three different Reynolds numbers based on the annular gap viz. Re = 10, 1 and 0.1.

Figure 4b reveals that the local maximum divergence over the entire computational domain is confined to the order of 10^{-4}, which is an acceptable mass conservation error in most numerical setups. It is pertinent to mention here that the underlying lattice-Boltzmann algorithm is susceptible to compressibility errors emerging from density variation and velocity divergence terms in the recovered Navier-Stokes' equation due to adoption of *pseudo-equation of state,* $p = \rho c_s^2$, and thereby deviates from a true solenoidal divergence [32]. These effects are, however, negligible if the density variations are small and thermodynamic considerations are not significant.

It must also be emphasized that although the lattice-Boltzmann equation recovers Navier–Stokes' equation in the incompressible limit, density cannot be kept constant in LB simulations as otherwise, the pressure changes cannot be captured. Hence, it is necessary to analyze also the effect of compressibility in present simulations, and we attempt to quantify the compressibility effects through the mean density fluctuation given by

$$\Delta = \frac{1}{\overline{\rho}}\sqrt{\sum (\rho - \overline{\rho})^2 / N} \tag{25}$$

where $\overline{\rho}$ is the mean density variation defined as,

$$\overline{\rho} = \frac{\sum_{x,y} \rho(x, y, t)}{N} \tag{26}$$

The compressibility and mass flux errors from the simulations using the DF-IB-LB method for a fixed value of $\tau = 1.0$ and different Re are summarized in Table 1. It is evident that both these quantities decrease with grid refinement, although the rate of decrease in compressibility error is approximately linear for the lowest value of Re. The dependence of τ on the compressibility and mass flux errors are best understood from Fig. 5 which shows that both errors increase with Re (for a given τ) and also exhibit an increase with τ for a given Reynolds number, keeping the grid size fixed. The errors in mass conservation and compressibility are therefore dependent on the grid size, choice of τ, and the flow Reynolds number, and care must be taken to keep these errors within acceptable limits for high Re flows. The fact that they decay with grid refinement affirms that the DF-IB-LB approach is discretely conservative in the limit of lattice size approaching zero. Although not shown herein, negligible velocity magnitudes of the order of 10^{-3} are observed outside the flow domain, in the vicinity of the curved boundaries, indicative of the fact that the no-slip boundary condition is approximately enforced despite the channel boundaries being non-aligned to the underlying Cartesian mesh.

Table 1 Compressibility and mass flux error for a flow through curved channel at different Re and grid resolution at a fixed $\tau = 1.0$

Domain size	Compressibility error	Mass flux error
Re = 10		
400 × 400	1.44E−3	7.37E−3
500 × 500	9.44E−4	4.89E−3
600 × 600	6.64E−4	3.48E−3
800 × 800	3.79E−4	2.03E−3
Re = 1		
400 × 400	1.49E−4	7.71E−5
500 × 500	9.98E−5	5.25E−5
600 × 600	7.35E−5	3.76E−5
800 × 800	2.17E−5	1.34E−5
Re = 0.1		
400 × 400	8.26E−6	5.31E−7
500 × 500	1.79E−5	9.92E−7
600 × 600	1.46E−5	8.88E−7
800 × 800	1.12E−5	7.67E−7

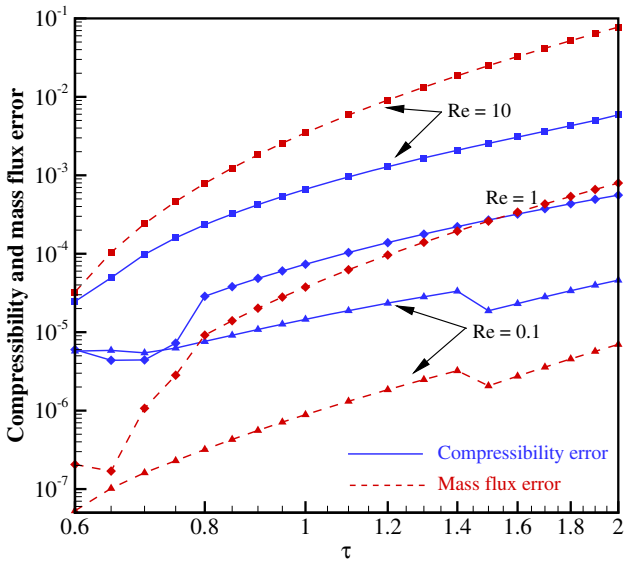

Fig. 5 Variation of compressibility and mass flux error with respect to τ for a flow inside curved channel at Re = 10, 1 and 0.1 for domain size 600 × 600

3.2 Accuracy study

The well-known Taylor–Couette problem is a classical test case often used to establish the accuracy of moving boundary problems as it constitutes both stationary and moving complex boundaries that are not aligned with the underlying Cartesian mesh. The fact that this flow field has an exact analytical solution makes it an ideal validation case for spatial accuracy studies. In our study, we choose two concentric cylinders of radii $R_1 = 0.2L$ and $R_2 = 0.4L$ that are

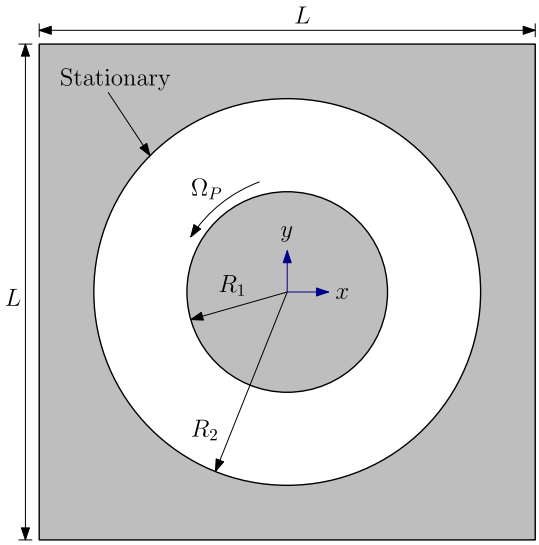

Fig. 6 Schematic for Taylor–Couette problem

immersed into a square computational domain of side $L = 1$ as represented in Fig. 6. The inner cylinder is subjected to a constant angular velocity $\vec{\Omega}_p = \vec{U}/R_1$, while the outer cylinder is static. The computational domain boundaries are prescribed as no-slip walls, and impermeable cylinder surfaces should restrict the flow only inside the annular region. The exact steady-state solutions of the flow field in terms of velocity, pressure, and driving torque associated with the rotatory motion are known

$$\vec{u}\,(x,\,y) = -\frac{\vec{\Omega}_P R_1^2}{R_2^2 - R_1^1}\left(\frac{R_2^2}{r^2} - 1\right) y \tag{27a}$$

$$\vec{v}\,(x,\,y) = -\frac{\vec{\Omega}_P R_1^2}{R_2^2 - R_1^1}\left(\frac{R_2^2}{r^2} - 1\right) x \tag{27b}$$

$$p\,(x,\,y) = \left[\frac{\vec{\Omega}_P R_1^2}{\left(R_2^2 - R_1^2\right)}\right]^2 \left\{\frac{r^2}{2} - \frac{R_2^4}{2r^2} - R_2^2 \log\left(r^2\right)\right\} \tag{27c}$$

$$\vec{T} = -4\pi\rho\nu\left[\frac{\vec{\Omega}_P R_1^2 R_2^2}{R_2^2 - R_1^2}\right] \tag{27d}$$

where $\vec{r} = \sqrt{x^2 + y^2}$ represents the position vector. Four different grid resolutions are considered to facilitate the order of accuracy analysis, viz. $\Delta x = L/40,\, L/80,\, L/160$, and $L/320$, while maintaining identical $\mathrm{Re} = U(2R_1)/\nu$ and convergence criterion of 10^{-8} for steady-state computations.

The rates of error decay with respect to grid refinement at $\tau = 0.6$ and 1.0 are expressed in terms of experimental order of convergence (EOC) in Table 2. Both L_∞ and L_2 error norms for velocity errors decay approximately linearly with grid refinement with the average EOC being 0.892 and 1.056 for $\tau = 0.6$ and 0.918 and 0.978 for $\tau = 1.0$ respectively.

Table 2 Experimental order of convergence (EOC) obtained by L_∞ and L_2 error norms of velocity and pressure for Taylor Couette problem at Re = 10

	Velocity error		Pressure error	
	L_∞	L_2	L_∞	L_2
$\tau = 0.6$				
$EOC_{40,80}$	0.820	0.972	1.727	1.678
$EOC_{80,160}$	0.890	0.968	1.749	1.736
$EOC_{160,320}$	0.967	1.229	1.801	1.777
$\overline{EOC}$	0.892	1.056	1.759	1.730
$\tau = 1.0$				
$EOC_{40,80}$	0.854	0.971	1.722	1.678
$EOC_{80,160}$	0.932	0.976	1.767	1.737
$EOC_{160,320}$	0.970	0.987	1.798	1.777
$\overline{EOC}$	0.918	0.978	1.763	1.731

The first order decline in velocity errors can be attributed to the presence of discontinuity in velocity gradients on the fluid–solid interface of IB-LB methods [20,33,34]. However, the pressure error exhibits nearly quadratic decay with grid refinement having an average EOC around 1.7, independent of the value of τ. From Table 3, one can also infer that the compressibility and mass flux errors decrease with grid refinement. The decay of compressibility error with respect to the computational Mach number is observed to be quadratic for both the cases of τ considered, while the relative torque error reduces with grid refinement at a rate of approximately first order.

In order to establish the dependence of relaxation factor (τ) on error norms of the DF-IB-LB method, we fixed the grid resolution at $\Delta x = {}^{L}/_{80}$ and varied τ from 0.6 to 2.0. Figure 7 reveals that velocity error norms decrease with increase in τ until $\tau = 1.5$ beyond which they exhibit an

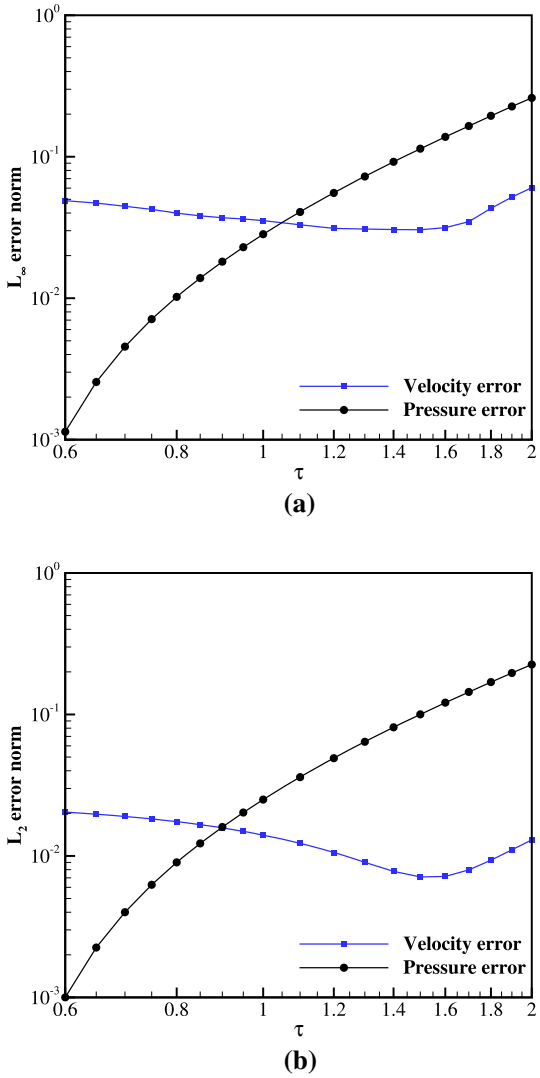

Fig. 7 Velocity and pressure error norms with respect to varying τ for Taylor Couette problem at Re = 10. **a** L_∞ error norm, **b** L_2 error norm

Table 3 Relative % torque error, compressibility error and mass flux error for Taylor Couette problem at Re = 10

Δx	Relative % torque error	Compressibility error	Mass flux error
$\tau = 0.6$			
$^1/_{40}$	13.169	2.50E−4	4.26E−7
$^1/_{80}$	6.624	5.75E−5	3.88E−8
$^1/_{160}$	3.091	1.38E−5	4.18E−9
$^1/_{320}$	1.982	3.37E−6	4.98E−10
$\tau = 1.0$			
$^1/_{40}$	9.276	5.96E−3	2.77E−5
$^1/_{80}$	4.013	1.40E−3	4.72E−6
$^1/_{160}$	2.029	3.40E−4	5.44E−7
$^1/_{320}$	1.044	8.38E−5	6.56E−8

increasing trend. The pressure error norms, however, exhibit a monotonic increase in magnitude with the increasing τ. The mass flux error is reasonably low for smaller values of τ but increases quite rapidly, as can be seen from Fig. 8a, as does the compressibility error. Interestingly, the relative torque error in Fig. 8b shows a local minimum at $\tau = 1.6$. While these results do not provide any clear guidelines on choosing an optimal value for τ, a choice of $\tau \leq 1.6$ is expected to keep the conservation errors to a minimum while computing the flow field accurately. Indeed, the solutions from the DF-IB-LB method exhibit an excellent degree of conformity with the exact velocity profiles, as shown in Fig. 9. The DF-IB-LB method in this work can be therefore considered as spatially first-order accurate with acceptable mass errors that is capable of accurately dealing with moving complex geometries.

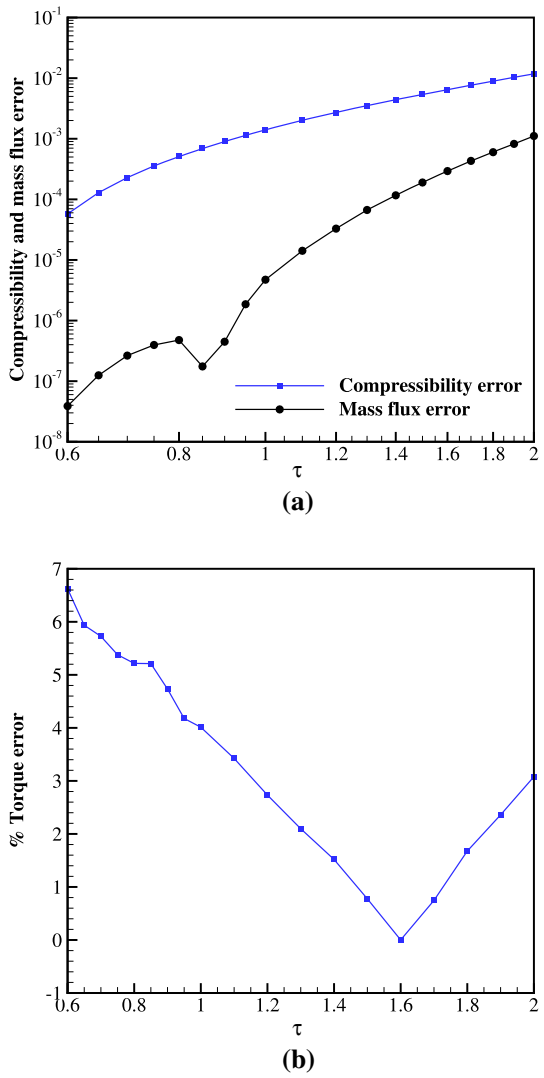

Fig. 8 **a** Compressibility and mass flux error, **b** relative % torque error with respect to varying τ for Taylor Couette problem at Re = 10

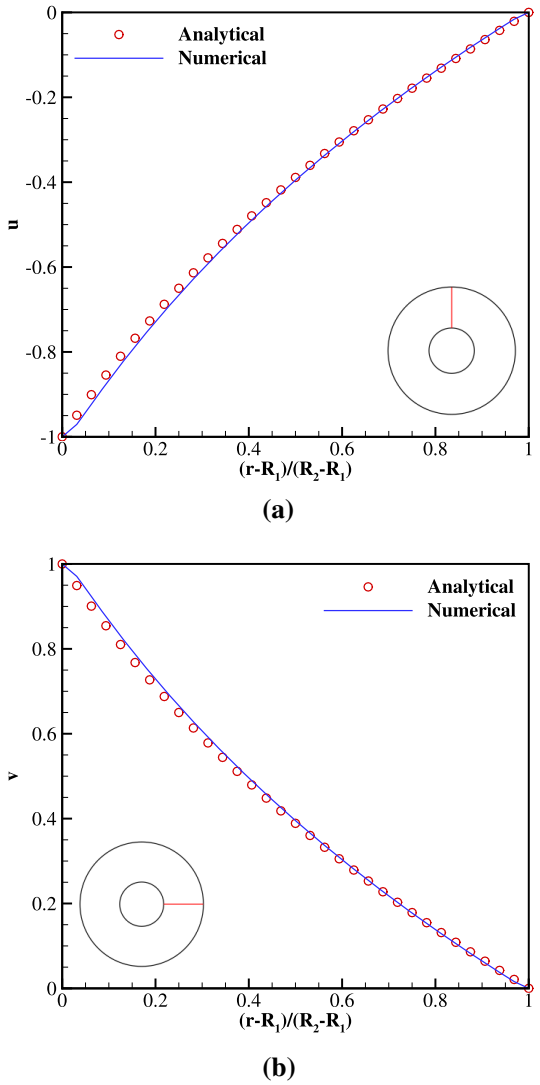

Fig. 9 Comparison of numerical and analytical solutions of velocity profiles of Taylor Couette problem at Re = 10: **a** u-velocity profile at $x = 0$ and **b** v-velocity profile at $y = 0$. The respective location of abscissa are represented in the inset

3.3 Galilean invariance study

We study Galilean invariance in the context of the DF-IB-LB approach, which is important given that conventional approaches with momentum-exchange method [29] in LBM at the fluid–solid interface are known to exhibit non-Galilean invariance behavior. While there have been algorithmic improvements for the momentum-exchange method [35,36], there have been no such studies forthcoming in the DF-IB-LB framework. The Galilean invariance study ensures that the method will yield an identical flow field irrespective of using a stationary or moving reference frame. Or in other words, the underlying computational framework is independent of the choice of reference frame for a moving body problem. Toward this objective, we consider the test case of the transient Couette flow past a moving cylinder inspired by the work of Lallemand and Luo [24]. A circular cylinder with diameter d is eccentrically placed in a channel of domain size $8d \times 4d$ as shown in Fig. 10. We consider two inertial frames in the study, with the first being a stationary (rest frame) where the initial flow field (U_0) and the moving cylinder (U_c) velocities in x-direction are prescribed as 0.02 m/s. The upper and bottom walls (U_w) of the channel are moving with a constant velocity of 0.1 m/s opposite to each other in x-direction. At LB-level, no-slip boundary conditions on channel walls are implemented using the non-equilibrium bounce back method proposed by Zou and He [37] while in x-direction periodic boundary conditions are applied. The second scenario is the moving reference frame with a constant reference velocity ($U_{\text{ref}} = -0.02$ m/s in x-direction. The cylinder thus becomes static with

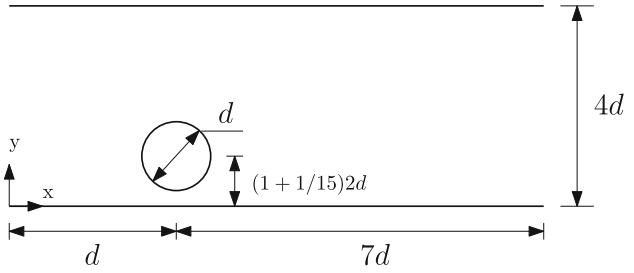

Fig. 10 Cylinder in a Couette flow

$U_c + U_{\text{ref}} = 0.0$ m/s and the initial condition of flow field becomes quiescent $U_0 + U_{\text{ref}} = 0.0$ m/s as well. The upper wall gains a velocity of $U_w + U_{\text{ref}} = 0.08$ m/s, while the velocity of the bottom wall becomes $U_w + U_{\text{ref}} = -0.12$ m/s. The simulation parameters for either scenarios are set as $\text{Re} = {}^{d^2\kappa}/_{\nu} = 11.36$, $\tau = 0.714$ and physical diameter of the cylinder as $d = 0.05m$. We choose the shear rate of the flow $\kappa = {}^{2U_w}/_{4d}$ where ν represents the kinematic viscosity of the fluid. The L_2 error norm for any quantity χ (like aerodynamic forces and torque), used to evaluate grid errors and Galilean invariance errors, is defined as:

$$L_2(\chi) = \sqrt{\frac{\sum_{n=0}^{N}\left[\chi^{\text{ref}}(t_n) - \chi(t_n)\right]^2}{\sum_{n=0}^{N}\left[\chi^{\text{ref}}(t_n)\right]^2}} \tag{28}$$

where N and χ^{ref} represent, respectively, the number of time steps and the reference solution considered for the analysis.

We evaluate the grid errors only for the moving reference frame case, whereas the Galilean invariance errors are evaluated for the rest reference frame. The resulting solution from the finest grid resolution of the moving reference frame case is selected as the reference solution ($\chi^{\text{ref}}(t_n)$) for grid errors. For Galilean invariance errors, the corresponding solution at the same grid resolution in the moving reference frame is set as the reference solution ($\chi^{\text{ref}}(t_n)$). The error analyses are facilitated by varying the number of lattice nodes on the diameter of the cylinder viz. 20, 40, 80, and 160. Figure 11 shows the grid errors and Galilean invariance errors for aerodynamic forces and torque with respect to grid resolution (Δx). The global error (gerr(L_2)) is evaluated as average of L_2 error norms of aerodynamic forces in x and y-direction. The grid errors are found to decay super linearly with grid refinement, while the Galilean invariance errors decay linearly with grid refinement. The time history of aerodynamic force coefficients, as shown in Fig. 12, reveals that the moving boundary case (i.e., the rest reference frame) exhibits fluctuations, which are, however, not very significant and decay with grid refinement. In a nutshell, it clearly demonstrates that the present DF-IB-LB method is a Galilean invariant method indeed for a sufficiently fine mesh.

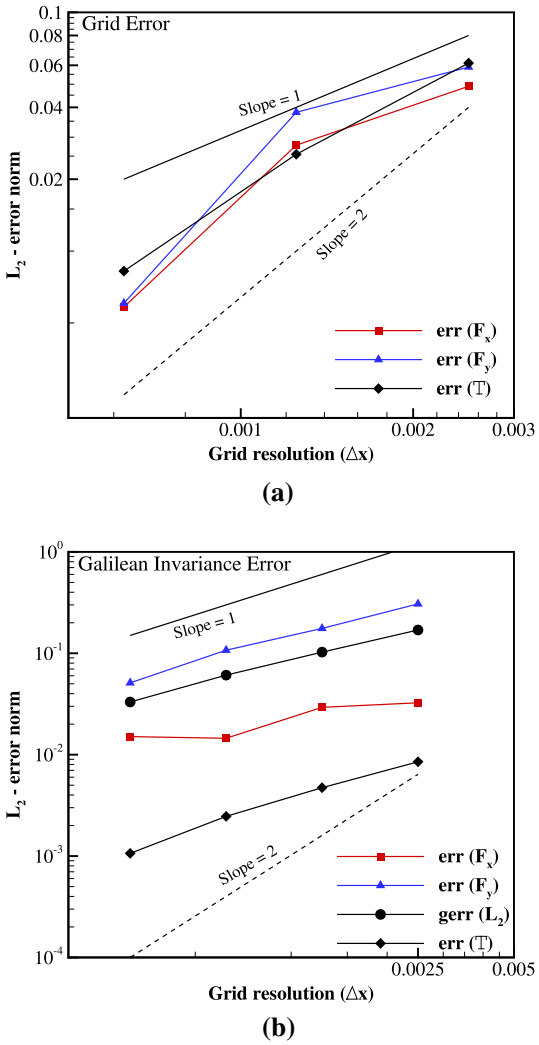

Fig. 11 Error norms of aerodynamic forces and torque for a cylinder in a Couette flow at Re = 11.36 and $\tau = 0.714$. **a** Grid error in a moving reference frame and **b** Galilean invariance error in static reference frame

3.4 Studies on spurious force oscillations

Spurious force oscillations (SFOs) in temporal histories of force coefficients are a major issue pertaining to moving boundary problems. While a body is in motion, the underlying lattice nodes experience a change in identity due to the birth and death of solid-fluid nodes. This identity transformation is often neither continuous nor smooth and can be attributed as the primary cause of SFOs. Kang [14] reported the presence of SFO in force signals for sharp-interface IB-LB schemes and mitigated the same by using standard smoothing or FFT filtering techniques. Although there were no specific comments on SFOs in the direct forcing approach in their studies, it was reported that the approach led to overprediction of the surface force coefficients. Several other studies [20,38] have reported the presence of SFOs in the

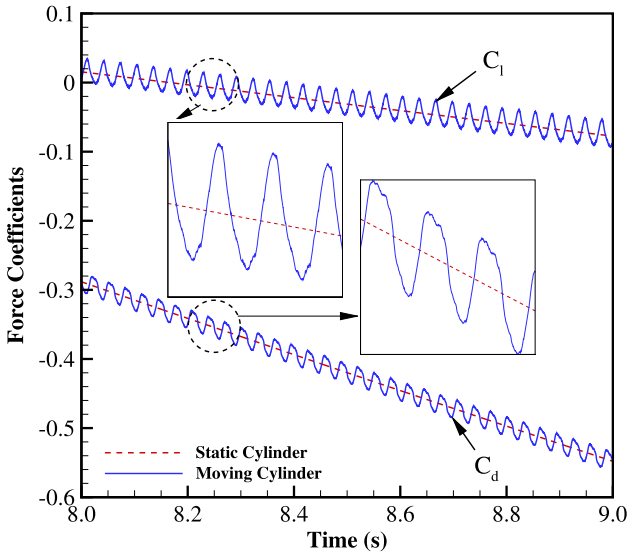

Fig. 12 Time variation of aerodynamic force coefficients of a cylinder in a Couette flow in moving and static reference frames at Re = 11.36 and $\tau = 0.714$

IB-LB methods, and we quantitatively probe these oscillations as a function of grid resolution in this work.

To facilitate this study, a circular cylinder of diameter d is subjected to an oscillatory motion within an initially quiescent computational domain of size $4d \times 4d$. The cylinder's motion about the geometrical center of the domain and its corresponding velocity in x-direction are given as:

$$X_c(t) = X_{c0} + A\,[1 - \cos(2\pi f t)]\,,$$
$$u_c(t) = U_0 \sin(2\pi f t) \tag{29}$$

where A, f, X_{c0} and U_0 represent the amplitude and frequency of oscillations, initial position of the cylinder and maximum cylinder velocity, respectively.

The simulation parameters are set identical to those in Seo and Mittal [39], whilst prescribing $A = 0.05d$, corresponding Reynolds number ($\mathrm{Re} = U_0 d/\nu$) and Strouhal number ($st = fd/U$)) as 31 and 3.2, respectively. Neumann boundary conditions with zero velocity gradient are prescribed on all boundaries of the domain using non-equilibrium bounce-back scheme [37]. Two sources of spurious fluctuations [40] pertaining to diffuse interface IB methods are attributed to spatial discontinuity in pressure across the immersed surface in newly born fluid nodes and the temporal discontinuity in velocity of dead fluid nodes. The spurious oscillations are comparatively more significant in pressure transients than the viscous forces and hence may be quantified using the 2δ-discontinuity in the temporal history of the pressure drag coefficients as [39]:

$$C_{\mathrm{PD}}^{2\delta} = |C_{\mathrm{PD}}^{n+1} - 2C_{\mathrm{PD}}^{n} + C_{\mathrm{PD}}^{n-1}| \tag{30}$$

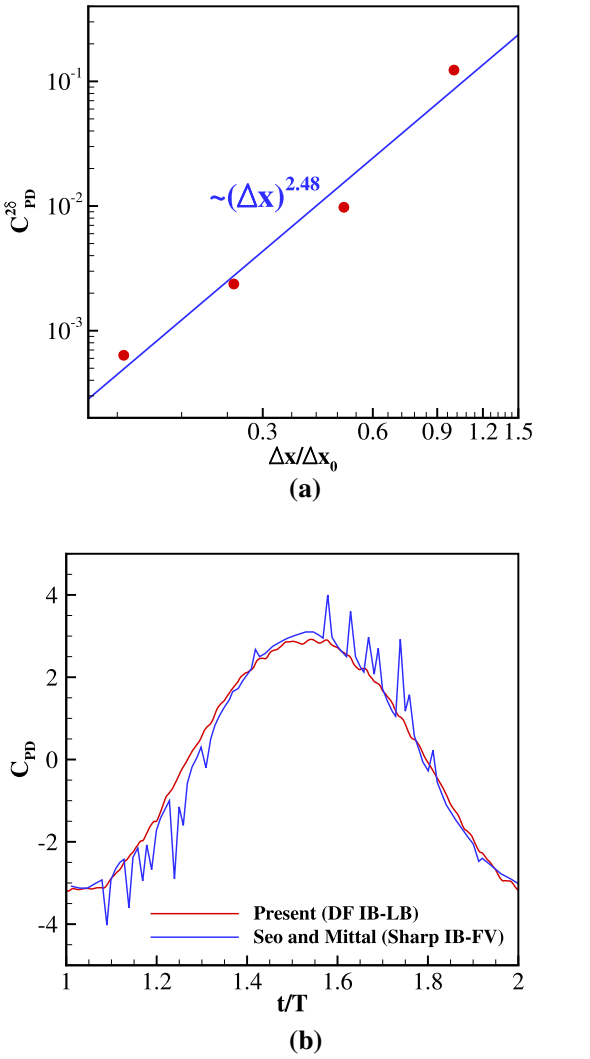

Fig. 13 **a** $C_{\mathrm{PD}}^{2\delta}$ discontinuity as a function of grid resolution. **b** Comparison of spurious fluctuation in pressure drag coefficient C_{PD} of present method with Seo and Mittal [39]

with n being time-step index. In our study, the grid resolutions are varied as $\Delta x/d = 1/16, 1/32, 1/64$ and $1/128$ while maintaining constant relaxation factor $\tau = 0.65$.

Figure 13a depicts the root-mean-square values of 2δ-discontinuity in pressure drag coefficient, where Δx_0 represents the coarsest grid resolution ($d/16$). The best-fit power-law curve through the discrete values reveals that $C_{\mathrm{PD}}^{2\delta}$ decays approximately at a rate of 2.48 which is higher than near-quadratic decay reported by Seo and Mittal [39] for sharp-interface immersed boundary-finite volume (IB-FV) method and approximately a linear decay ($C_{\mathrm{PD}}^{2\delta} \sim (\Delta x)^{1.31}$) using a volume-of-body IB-FV solver [41]. The comparison of temporal history of pressure drag coefficient (C_{PD}) with sharp-interface IB-FV [39] (as shown in Fig. 13b) and different grid resolutions (as shown in Fig. 14) further confirms the efficacy of DF-IB-LB towards smooth estimation of aero-

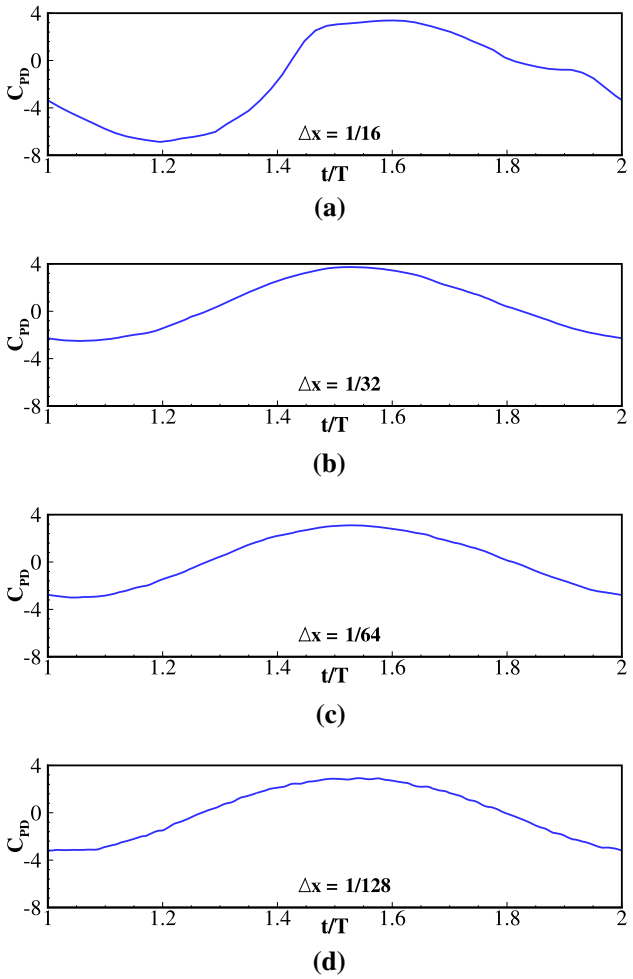

Fig. 14 Temporal history of pressure drag coefficient (C_{PD})

dynamic forces in moving boundary problems. This analysis shows that the SFOs diminish very rapidly on finer meshes, and no separate treatment is necessary to ensure that the time histories of lift and drag coefficients are smooth. This is particularly important when fluid forces influence the motion of the structure, such as in the problems of vortex-induced vibrations and sedimentation, with the latter being investigated in detail later in this work. Importantly, compared to sharp interface IB approaches such as those of Seo and Mittal [39], the DF-IB-LB approach has much fewer oscillations on a given mesh owing to the smoothening of the interface, but this does not compromise the accuracy of solutions in practical flow problems as demonstrated by our investigations in the following section.

4 Simulations of incompressible flow problems using DF-IB-LB solver

The preceding section has established the DF-IB-LB method as a nominally first-order accurate approach which is Galilean invariant and has acceptably low conservation errors and tolerable SFOs. The ease of implementation of the approach, along with these desirable features, motivates a thorough investigation of the method for a broad spectrum of test cases encompassing imposed and induced motion of structures in moving boundary scenarios. We must also remark that grid independence studies have been conducted for all test cases discussed below, and all computations are necessarily grid-independent.

4.1 Flow induced by inline oscillating cylinder

The first test case we consider is the inline oscillation of a circular cylinder of diameter d in a quiescent computational domain of dimensions $30d \times 20d$ as shown in Fig. 15a. A harmonic oscillation in x-direction is imposed on the cylinder as:

$$X_c(t) = X_{c,0} - A\sin(2\pi f t) \tag{31}$$

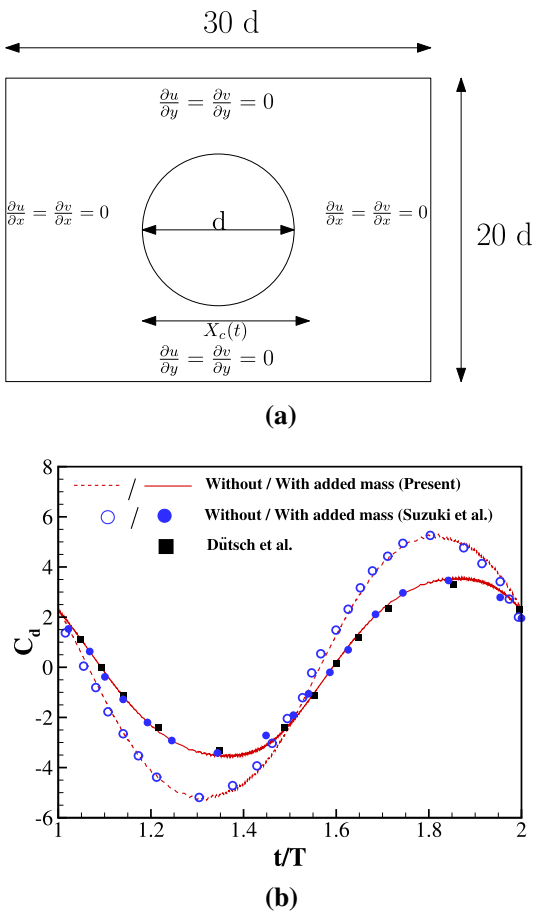

Fig. 15 **a** Schematic of an inline oscillating cylinder and **b** Comparison of coefficient of drag of present solver with literature [42,43] for inline oscillating cylinder at Re = 100 and KC = 5

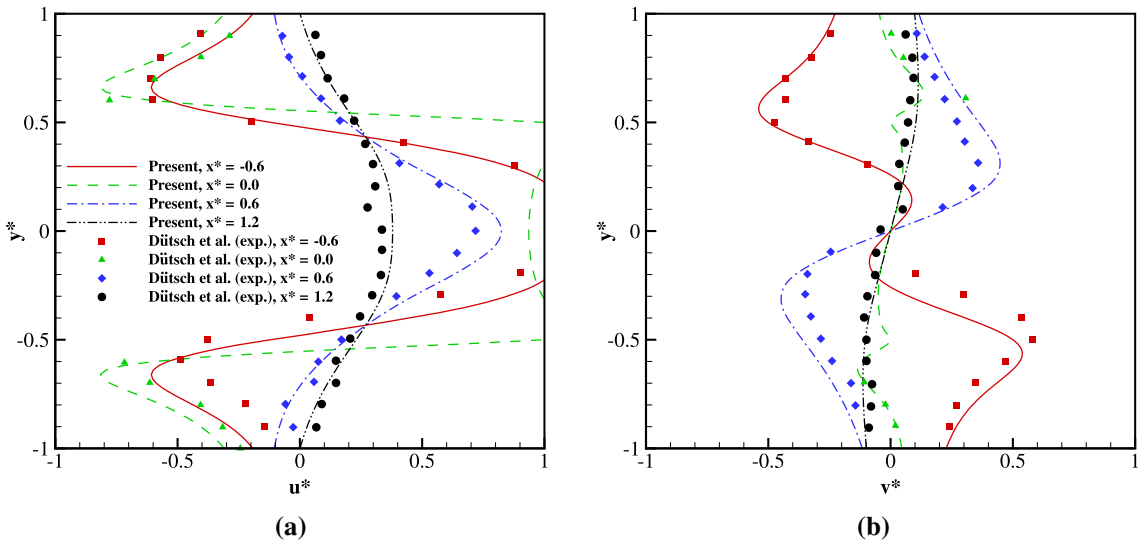

Fig. 16 Comparison of velocity profile between the present work and experimental data obtained by Dütsch et al. [43] at phase angle 180° for Re = 100 and KC = 5. x^* and u^* represents the non-dimensionalized position and velocity respectively

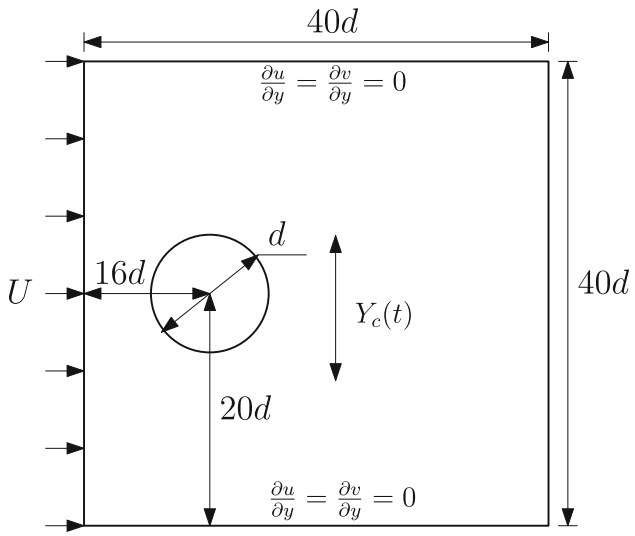

Fig. 17 Schematic of a transversely oscillating cylinder

where the notations have similar meaning to those used in Eq. (29).

On the domain boundaries, Neumann boundary conditions are prescribed while the cylinder surface is impermeable. We study the test case for Reynolds number (Re $= U_0 d/\nu$) = 100 and Keulegan–Carpenter number (KC $= U_0/fd$) $= 5$. The LB simulation parameters are set as $\tau = 0.65$ and 50 lattice nodes over cylinder diameter. A vital aspect pertinent to moving boundary problems, as detailed previously, involves estimating the temporal history of aerodynamic force signals. Figure 15b reveals an excellent agreement of time history of drag coefficient of present solver with those of Suzuki and Inamuro [42] and Dütsch et al. [43]. Furthermore, Fig. 15b also suggests that the inclusion of added mass term in particle dynamics formulation is imperative for high Re flows as presented in Sect. 2.3. It is evident that neglecting the added mass term leads to inaccurate prediction in the force coefficients. The capability of the present solver to capture accurate local hydrodynamic signals is also clear from the compari-

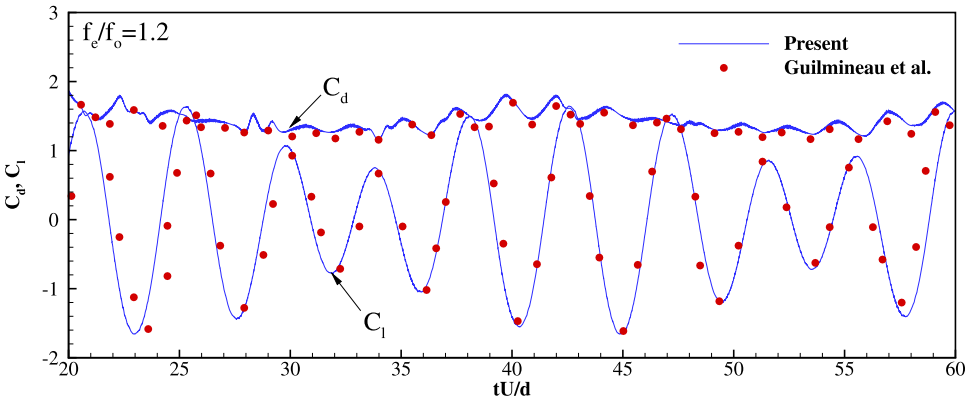

Fig. 18 Time history of aerodynamic coefficients of a transversely oscillating cylinder at frequency ratio 1.2 and its comparison with Guilmineau and Queutey [44]

Table 4 Comparison of aerodynamic force coefficients of present work with literature [44–46] at different frequency ratio and Re = 185

	Present	Guilmineau and Queutey [44]	Wang et al. [45]	Chen et al. [46]
$f_e/f_o = 0.8$				
$C_{d,\text{rms}}$	0.0447	0.0414	0.0384	0.0357
$C_{l,\text{rms}}$	0.0744	0.0800	0.0795	0.0714
$< C_d >$	1.2770	1.1986	1.2301	1.3036
$f_e/f_o = 1.0$				
$C_{d,\text{rms}}$	0.1474	0.1357	0.1370	0.1310
$C_{l,\text{rms}}$	0.4155	0.4186	0.3836	0.3393
$< C_d >$	1.5885	1.4986	1.5590	1.6250
$f_e/f_o = 1.2$				
$C_{d,\text{rms}}$	0.1364	0.1271	0.1370	0.1369
$C_{l,\text{rms}}$	0.9493	0.9329	0.9589	0.9643
$< C_d >$	1.4098	1.3486	1.3986	1.4940

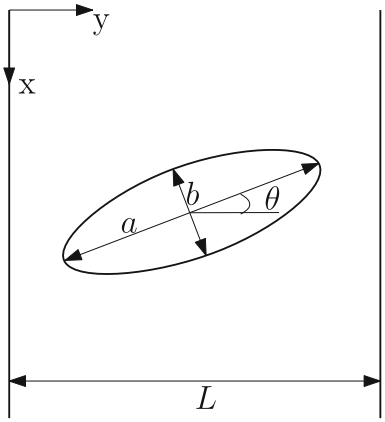

Fig. 19 Schematic of an elliptical particle sedimentation

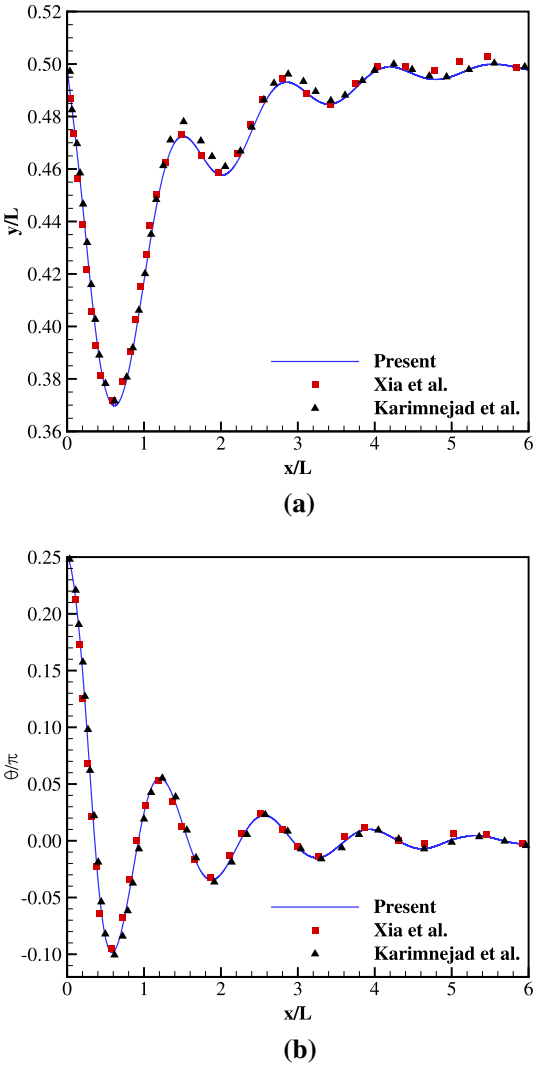

Fig. 20 Comparison of particle trajectory and its orientation of the present work with Xia et al. [47] and Karimnejad et al. [48]

son of velocity profiles with experimental data obtained by Dütsch et al. [43] as illustrated in Fig. 16.

4.2 Flow past a transverse oscillating cylinder

We consider another imposed motion test case in this section where we study the transverse oscillation of a cylinder in a flow field. A circular cylinder of diameter d is subjected to a sinusoidal motion (Eq. 32) in y-direction in a computational domain of size $40d \times 40d$ as shown in Fig. 17.

$$Y_c(t) = Y_{c,0} - A\sin(2\pi f_e t) \tag{32}$$

Here, the quantities Y_c, $Y_{c,0}$, A and f_e represent the instantaneous position of the cylinder, initial position at $t = 0$, amplitude of oscillation ($= 0.02d$) and excitation frequency of oscillations respectively. A uniform velocity at the inlet corresponding to Re = 185 is prescribed while the outlet is maintained at constant pressure. Neumann boundary conditions with zero velocity gradient are prescribed on the upper and lower boundaries of the computational domain. Studies are performed for several values of frequency ratio (f_e/f_0) viz. 0.8, 1.0 and 1.2, where f_0 refers to the natural vortex shedding frequency corresponding to Strouhal number ($St = 0.192$) obtained beforehand by simulating flow past a stationary circular cylinder at Re = 185.

The time history of aerodynamic force coefficients at $f_e/f_0 = 1.2$ (shown in Fig. 18) reveals a good agreement with results obtained by Guilmineau and Queutey [44], and no significant spurious pressure fluctuations are observed either using the DF-IB-LB method. The comparison of time-averaged coefficient of drag ($\leq C_d \geq$), RMS C_d and C_l listed in Table 4 at different frequency ratios further highlights the efficacy of the present solver to accurately predict complex

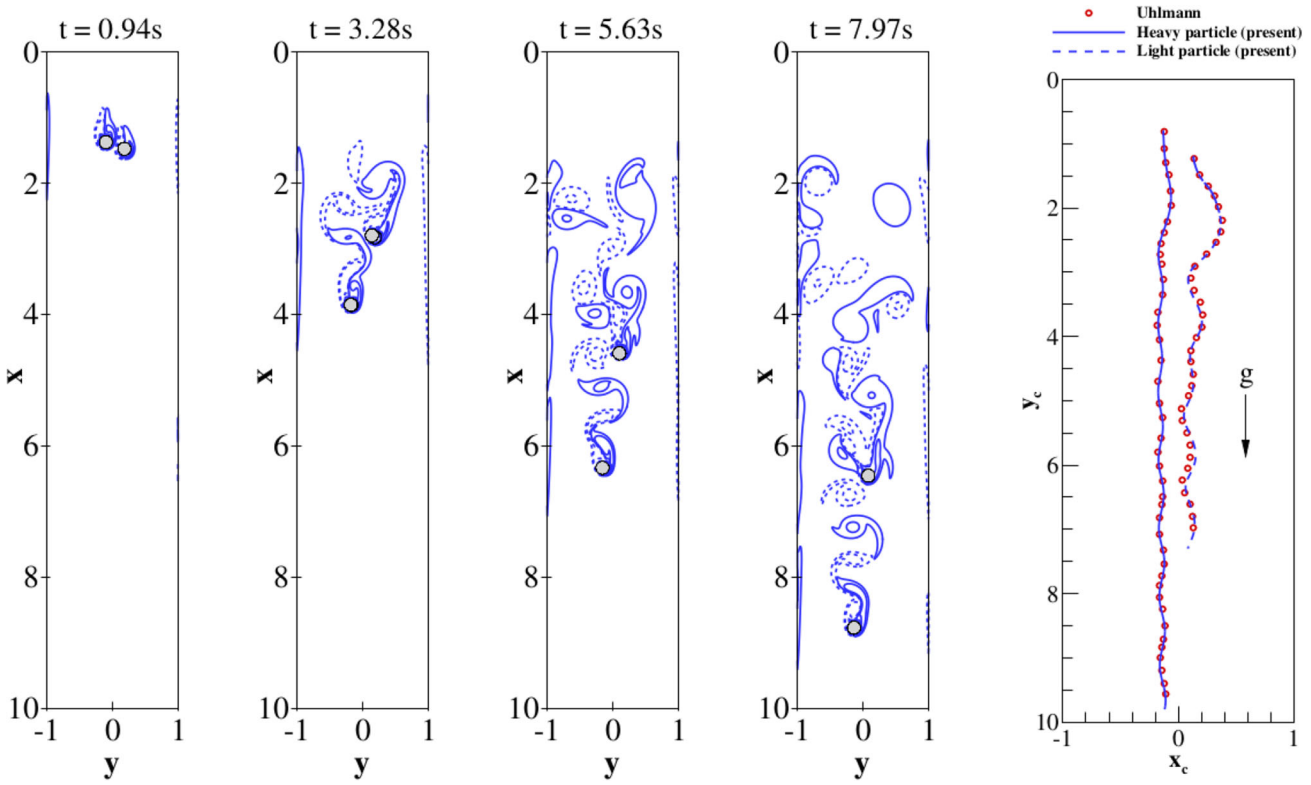

Fig. 21 Sedimentation of particles of different weight: instantaneous vorticity contours and trajectory of particles

hydrodynamics involving moving boundary problems with no issues of SFOs.

4.3 Sedimentation of an elliptical particle

Having explored the capability of the present solver for imposed motion problems, we now extend the solver to simulate fluid–particle interaction problems involving induced motion. As a first benchmark problem of this category, we select an elliptical body subjected to sediment freely under the influence of gravity. As compared to circular bodies considered so far, an ellipse can be considered a relatively complex structure, and the present problem will also put to the test the solver's capability and robustness in handling such geometries. The simulation parameters are chosen identical to those of Xia et al. [47], and as shown in Fig. 19 the physical dimensions of major and minor axes of the elliptical particle are chosen to be $0.1cm$ and 0.05 cm, respectively. We set the particle initially at rest in the middle of a narrow channel of width $L = 0.4$ cm, and to break the symmetry of the flow, the initial orientation of the particle is fixed as $\theta = \pi/4$. The solid-fluid density ratio (ρ_p/ρ_f) is taken as 1.1 and kinematic viscosity of the fluid (ν_f) is taken to be 0.01 cm^2/s. We choose 50 and 400 lattice nodes over the major axis of the particle and channel width, respectively, and using a relaxation factor of $(\tau) = 0.6364$ leads to a physical time step size $(\Delta t) = 1.82 \times 10^{-5}$ s for the simulation.

The particle trajectory and its orientation during the course of its travel are depicted in the Fig. 20. As the particle progresses on its journey towards the wall, it obtains sufficient repulsive force due to the wall effects and simultaneously changes its course of the journey toward the center of the domain. After several fluctuations, it finally settles to a stable position. The particle trajectories commensurate with the flow physics from the present numerical solver are in good agreement with the studies of Xia et al. [47] and Karimnejad et al. [48], indicative of the ability of the DF-IB-LB approach to compute unsteady flows past complex moving bodies.

4.4 Sedimentation of two particles of different weights

To examine the efficacy of the DF-IB-LB algorithm for fluid–particle interactions, we now consider the sedimentation of two circular particles of different weights. The two particles fall freely under the influence of gravity in a quiescent medium, but their trajectories are influenced by the flow dynamics, particle–particle, and particle–wall interactions. The problem statement for the test case is in coherence with that proposed by Uhlmann [49] comprising of identical circular particles of diameter $d = 0.2$, initially located

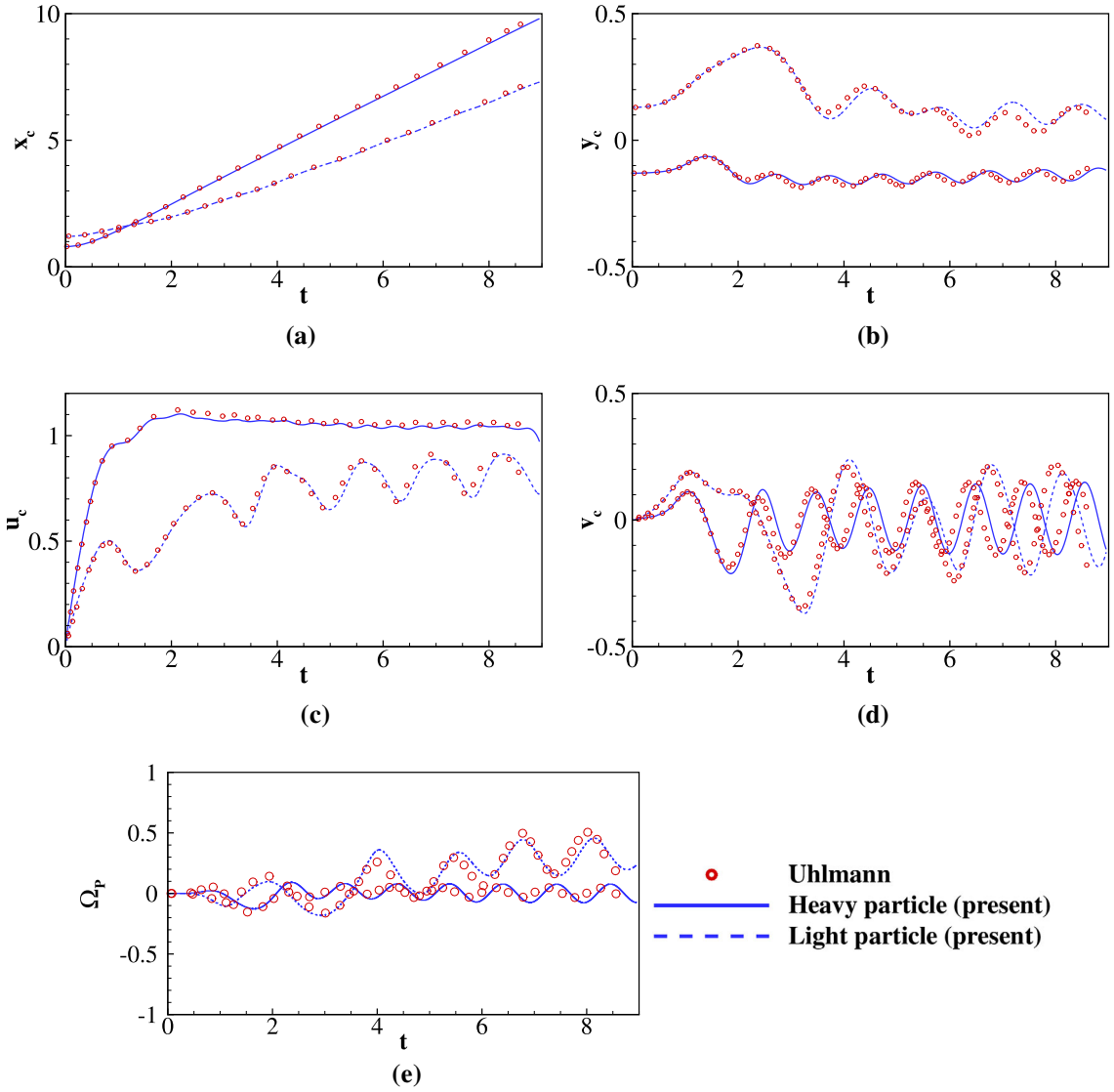

Fig. 22 Sedimentation of particles of different weight : time evolution of particles' **a**, **b** center location, **c**, **d** linear velocities and **e** angular velocity. Solid and dashed lines represent light and heavy particles, respectively, of the present work, whereas the circle symbol indicates the data of Uhlmann [49]

at $X_c^{(1)}|_{t=0} = (0.8, -0.13)$ and $X_c^{(2)}|_{t=0} = (1.2, 0.13)$ in a computational domain of dimension $[0, 10] \times [-1, 1]$. The particle-to-fluid density ratio of the particles are set as $\rho_p^{(1)}/\rho_f = 1.5$ and $\rho_p^{(2)}/\rho_f = 1.25$, respectively. The fluid kinematic viscosity is taken as $8 \times 10^{-4}\text{m}^2/\text{s}$ and a discrete domain of 4000×800 lattice-units corresponding to $\Delta x = \Delta y = 0.0025$ m units is chosen for the simulations. We consider $\tau = 0.59$ corresponding to a physical time step of 2.344×10^{-4} s and the lattice level gravity is 2.156×10^{-4} lattice-units. The simulations are carried out till the heavier particle reaches within $2d$ distance from the base of the computational domain. The maximum particle Reynolds number predicted using the present DF-IB-LB method for the particles are 276.61 and 231.41, which are very close to those computed by Uhlmann [49] (280 and 230, respectively).

Instantaneous vorticity contours shown in Fig. 21 depict that the heavier particle overtakes the lighter particle, and the trailing lighter particle moves into the wake region of the heavier one. Unlike the trajectory of the heavier particle, which is largely vertical, the lighter particle deviates from its vertical trajectory due to the strong interactions with the wake vortices, as observed in Fig. 21. In addition to the accurate prediction of the particle trajectories, the present results in Fig. 22 show an excellent agreement for the temporal history of translational and angular velocities as well. It can be inferred from these studies that the direct forcing IB-LB

method possesses the promising potential to simulate one or moving boundary problems and accurately capture the complex interplay between fluid and solids.

5 Conclusions

In this paper, we have investigated the efficacy of the direct-forcing immersed boundary–lattice Boltzmann (DF-IB-LB) for solving complex moving boundary problems with a particular focus on its accuracy, discrete conservation, Galilean invariance, and spurious force oscillations. The investigations on these aspects, which have not previously been carried out in the literature, show that the method is nominally first-order accurate with the diffusion of the interface significantly reducing the spurious oscillations for moving boundary problems. The method is shown to be Galilean invariant and mass-conservative in the limit of $\Delta x \longrightarrow 0$ with the errors decaying with mesh refinement. This study therefore provides some guidelines on the mesh spacing to be chosen to ensure acceptable mass and compressibility errors in moving boundary problems. The versatility of the solver is demonstrated using moving boundary problems involving complex hydrodynamics that include both imposed and induced motion. Our studies conclusively highlight that the DF-IB-LB approach is a promising alternative to simulate incompressible hydrodynamics, which may be extended to solve multi-component flows in the near future.

Acknowledgements S.M. and A.G. would like to express their gratitude to Ministry of Education (MoE), India, for the financial support during the course of this work. All the computations reported here are carried out in the PARAM-ISHAN cluster, a 162 nodes, 250 TFps hybrid high-performance computing facility at IIT Guwahati. Authors would also like to thank the anonymous reviewers whose comments have helped in improving the paper.

Declarations

Conflict of interest On behalf of all authors, the corresponding author states that there is no conflict of interest

References

1. Third JR, Chen Y, Müller CR (2015) Comparison between finite volume and lattice-Boltzmann method simulations of gas-fluidised beds: bed expansion and particle–fluid interaction force. Comput Part Mech 3(3):373–381
2. Esteghamatian A, Hammouti A, Lance M, Wachs A (2017) Particle resolved simulations of liquid/solid and gas/solid fluidized beds. Phys Fluids 29(3):033302
3. Nath G, Ray B, Sarkar J (2021) Self-assembly of amphiphilic Janus spheres using the lattice Boltzmann method. Comput Part Mech 9:67–83
4. Connington K, Kang Q, Viswanathan H, Abdel-Fattah A, Chen S (2009) Peristaltic particle transport using the lattice Boltzmann method. Phys Fluids 21(5):053301
5. Bakhshan M, Wörner M, Dadvand A (2021) Simulation of droplet impingement on a rigid square obstacle in a microchannel using multiphase lattice Boltzmann method. Comput Part Mech 8(4):973–991
6. Zhang L, Jebakumar AS, Abraham J (2016) Lattice Boltzmann method simulations of stokes number effects on particle motion in a channel flow. Phys Fluids 28(6):063306
7. Liu W, Wu C-Y (2019) Analysis of inertial migration of neutrally buoyant particle suspensions in a planar Poiseuille flow with a coupled lattice Boltzmann method-discrete element method. Phys Fluids 31(6):063301
8. Krzyzanowski M, Svyetlichnyy D (2021) A multiphysics simulation approach to selective laser melting modelling based on cellular automata and lattice Boltzmann methods. Comput Part Mech 9:117–133
9. Leonardi A, Wittel FK, Mendoza M, Herrmann HJ (2014) Coupled DEM-LBM method for the free-surface simulation of heterogeneous suspensions. Comput Part Mech 1(1):3–13
10. Tao S, He Q, Chen B, Qin FGF (2020) Distribution function correction-based immersed boundary lattice Boltzmann method for thermal particle flows. Comput Part Mech 8(3):459–469
11. Wang M, Feng YT, Wang Y, Qu TM, He W (2019) A hybrid discrete bubble-lattice Boltzmann–discrete element model for gas-charged sediments. Comput Part Mech 7(3):509–522
12. Rezaee T, Sadeghy K (2019) Effect of porosity on the settling behavior of a 2d elliptic particle in a narrow vessel: a lattice-Boltzmann simulation. Phys Fluids 31(12):123301
13. Mittal R, Iaccarino G (2005) Immersed boundary methods. Annu Rev Fluid Mech 37(1):239–261
14. Kang SK (2010) Immersed boundary methods in the lattice Boltzmann equation for flow simulation. PhD thesis
15. Feng ZG, Michaelides EE (2004) The immersed boundary–lattice Boltzmann method for solving fluid–particles interaction problems. J Comput Phys 195(2):602–628
16. Feng ZG, Michaelides EE (2005) Proteus: a direct forcing method in the simulations of particulate flows. J Comput Phys 202(1):20–51
17. Niu XD, Shu C, Chew YT, Peng Y (2006) A momentum exchange-based immersed boundary–lattice Boltzmann method for simulating incompressible viscous flows. Phys Lett A 354(3):173–182
18. Wu J, Shu C (2009) Implicit velocity correction-based immersed boundary–lattice boltzmann method and its applications. J Comput Phys 228(6):1963–1979
19. Noble DR, Torczynski JR (1998) A lattice-Boltzmann method for partially saturated computational cells. Int J Mod Phys C 09(08):1189–1201
20. Zhang C, Cheng Y, Zhu L, Wu J (2016) Accuracy improvement of the immersed boundary–lattice Boltzmann coupling scheme by iterative force correction. Comput Fluids 124:246–260
21. Dupuis A, Chatelain P, Koumoutsakos P (2008) An immersed boundary–lattice-boltzmann method for the simulation of the flow past an impulsively started cylinder. J Comput Phys 227(9):4486–4498
22. Krüger T, Kusumaatmaja H, Kuzmin A, Shardt O, Silva G, Viggen EM (2016) The lattice Boltzmann method principles and practice. Graduate texts in physics. Springer, Berlin
23. Filippova O, Hanel D (1998) Grid refinement for lattice-BGK models. J Comput Phys 147(1):219–228
24. Lallemand P, Luo L-S (2003) Lattice Boltzmann method for moving boundaries. J Comput Phys 184(2):406–421
25. Zhao-Li G, Chu-Guang Z, Bao-Chang S (2002) Non-equilibrium extrapolation method for velocity and pressure boundary conditions in the lattice Boltzmann method. Chin Phys 11(4):366–374

26. Peskin CS (2002) The immersed boundary method. Acta Numerica 11:479–517
27. Cheng Y, Zhu L, Zhang C (2014) Numerical study of stability and accuracy of the immersed boundary method coupled to the lattice Boltzmann BGK model. Commun Comput Phys 16(1):136–168
28. Ladd AJC (1994) Numerical simulations of particulate suspensions via a discretized Boltzmann equation. Part 2. Numerical results. J Fluid Mech 271:311–339
29. Mei R, Yu D, Shyy W, Luo L-S (2002) Force evaluation in the lattice Boltzmann method involving curved geometry. Phys Rev E 65:041203
30. Yin X, Le G, Zhang J (2012) Mass and momentum transfer across solid–fluid boundaries in the lattice-Boltzmann method. Phys Rev E 86:026701
31. Patel JK, Natarajan G (2018) Diffuse interface immersed boundary method for multi-fluid flows with arbitrarily moving rigid bodies. J Comput Phys 360:202–228
32. Nourgaliev RR, Dinh TN, Theofanous TG, Joseph D (2003) The lattice Boltzmann equation method: theoretical interpretation, numerics and implications. Int J Multiph Flow 29(1):117–169
33. Suzuki K, Inamuro T (2013) A higher-order immersed boundary–lattice Boltzmann method using a smooth velocity field near boundaries. Comput Fluids 76:105–115
34. Hu Y, Li D, Shu S, Niu X (2016) An efficient immersed boundary–lattice Boltzmann method for the simulation of thermal flow problems. Commun Comput Phys 20(5):1210–1257
35. Caiazzo A, Junk M (2008) Boundary forces in lattice Boltzmann: analysis of momentum exchange algorithm. Comput Math Appl 55(7):1415–1423 (Mesoscopic Methods in Engineering and Science)
36. Wen B, Zhang C, Tu Y, Wang C, Fang H (2014) Galilean invariant fluid–solid interfacial dynamics in lattice Boltzmann simulations. J Comput Phys 266:161–170
37. Zou Q, He X (1997) On pressure and velocity boundary conditions for the lattice Boltzmann BGK model. Phys Fluids 9(6):1591–1598
38. Chen L, Yu Y, Hou G (2013) Sharp-interface immersed boundary lattice Boltzmann method with reduced spurious-pressure oscillations for moving boundaries. Phys Rev E 87:053306
39. Seo JH, Mittal R (2011) A sharp-interface immersed boundary method with improved mass conservation and reduced spurious pressure oscillations. J Comput Phys 230(19):7347–7363
40. Lee J, Kim J, Choi H, Yang K-S (2011) Sources of spurious force oscillations from an immersed boundary method for moving-body problems. J Comput Phys 230(7):2677–2695
41. De AK (2018) A diffuse interface immersed boundary method for complex moving boundary problems. J Comput Phys 366:226–251
42. Suzuki K, Inamuro T (2011) Effect of internal mass in the simulation of a moving body by the immersed boundary method. Comput Fluids 49(1):173–187
43. Dütsch H, Durst F, Becker S, Lienhart H (1998) Low-Reynolds-number flow around an oscillating circular cylinder at low Keulegan–Carpenter numbers. J Fluid Mech 360:249–271
44. Guilmineau E, Queutey P (2002) A numerical simulation of vortex shedding from an oscillating circular cylinder. J Fluids Struct 16(6):773–794
45. Wang Y, Shu C, Teo CJ, Wu J (2015) An immersed boundary–lattice Boltzmann flux solver and its applications to fluid–structure interaction problems. J Fluids Struct 54:440–465
46. Chen Z, Shu C, Tan D (2018) Immersed boundary-simplified lattice Boltzmann method for incompressible viscous flows. Phys Fluids 30(5):053601
47. Xia Z, Connington KW, Rapaka S, Yue P, Feng JJ, Chen S (2009) Flow patterns in the sedimentation of an elliptical particle. J Fluid Mech 625:249–272
48. Karimnejad S, Amiri Delouei A, Nazari M, Shahmardan MM, Mohamad AA (2018) Sedimentation of elliptical particles using immersed boundary–lattice Boltzmann method: a complementary repulsive force model. J Mol Liq 262:180–193
49. Uhlmann M (2005) An immersed boundary method with direct forcing for the simulation of particulate flows. J Comput Phys 209(2):448–476